JOURNAL OF AIRCRAFT
Vol. 60, No. 4, July–August 2023

Check for updates

Finite Element Model Tuning Using Analytical Sensitivity Values

Chan-gi Pak*
NASA Armstrong Flight Research Center, Edwards, California 93523-0273

https://doi.org/10.2514/1.C037178

This paper presents an efficient approach for tuning finite element models to match the measured ground vibration test and proof test data. Frequencies, mode shapes, total weight, location of the center of gravity, and static deformation computed from the finite element model are matched to the measured data. The model tuning procedure used in this work is based on solving an optimization problem in which the errors for the considered metrics, between the finite element prediction and the measured data, are minimized. Analytical sensitivity values of performance indices are computed using the NASTRAN-generated sensitivity values together with the in-house computer programs, which allow for faster computational time and the use of gradient-based optimizers. The method is applied to the Aerostructures Test Wing 4 model. The study shows that the military standard and the NASA standard for comparing analytical and experimental modal data are all satisfied. The final finite element model correlates well with the test data. The flutter speed decreases by 8.91% after model tuning compared with the original Aerostructures Test Wing 4 design.

Nomenclature

F_{ir}	=	ith reference response function value for computation of ith performance index
$F_i(x_k)$	=	ith response function computed from NASTRAN solution 200
f_j	=	jth analytical frequency, Hz
f_{jg}	=	jth measured frequency, Hz
$\boldsymbol{I}$	=	identity matrix
I_{xxG}	=	moment of inertia I_{xx} with respect to center of gravity
I_{xxo}	=	moment of inertia I_{xx} with respect to origin
I_{yxG}	=	moment of inertia I_{yx} with respect to center of gravity
I_{yxo}	=	moment of inertia I_{yx} with respect to origin
I_{yyG}	=	moment of inertia I_{yy} with respect to center of gravity
I_{yyo}	=	moment of inertia I_{yy} with respect to origin
I_{zxG}	=	moment of inertia I_{zx} with respect to center of gravity
I_{zxo}	=	moment of inertia I_{zx} with respect to origin
I_{zyG}	=	moment of inertia I_{zy} with respect to center of gravity
I_{zyo}	=	moment of inertia I_{zy} with respect to origin
I_{zzG}	=	moment of inertia I_{zz} with respect to center of gravity
I_{zzo}	=	moment of inertia I_{zz} with respect to origin
J	=	objective function
J_i	=	ith performance indices
$\boldsymbol{M}_{\mathrm{AOM}}$	=	auto-orthogonality matrix
$\boldsymbol{M}_{\mathrm{COM}}$	=	cross-orthogonality matrix
$\boldsymbol{M}_R$	=	reduced-order mass matrix
m	=	number of modes to be matched
n_{FDOF}	=	number of full-order degrees of freedom
n_{MDOF}	=	number of measured degrees of freedom
n_{RDOF}	=	number of reduced degrees of freedom
$\boldsymbol{T}$	=	transformation matrix, full-order degrees of freedom to reduced-order degrees of freedom
W	=	total weight
W_G	=	measured total weight
x_{CG}	=	X-center-of-gravity location
x_k	=	kth design variable
x_{MCG}	=	measured X-center-of-gravity location
y_{CG}	=	Y-center-of-gravity location
y_{MCG}	=	measured Y-center-of-gravity location
z_{CG}	=	Z-center-of-gravity location
z_{MCG}	=	measured Z-center-of-gravity location
$\boldsymbol{\Phi}_{GR}$	=	expanded eigenmatrix
$\boldsymbol{\Phi}_M$	=	eigenmatrix, corresponds to master (or measured) degrees of freedom
$\boldsymbol{\Phi}_R$	=	eigenmatrix, corresponds to reduced degrees of freedom
$\boldsymbol{\Phi}_S$	=	eigenmatrix, corresponds to slave degrees of freedom
$\tilde{\boldsymbol{\Phi}}_{GM}$	=	measured eigenmatrix
$\boldsymbol{\Psi}$	=	intermediate matrix to compute M_R
$\boldsymbol{\Psi}_M$	=	intermediate matrix to compute Φ_{GR}
$\boldsymbol{\omega}_n$	=	natural frequency
$(*)^{\mathrm{T}}$	=	transpose of a matrix
$(*)^{-1}$	=	inverse of a matrix
$\partial(*)/\partial x_k$	=	sensitivity value with respect to the kth design variable x_k

I. Introduction

GENERALLY, structural dynamic finite element (FE) models for production aircraft need to be correlated to the measured data to ensure the accuracy of the numerical models. A trial-and-error approach for structural model tuning remains the most popular methodology in industry and government to save aircraft development schedule time between the ground vibration test (GVT) and the first flight test. The quality of the tuned FE model is, therefore, questionable for its use in predicting aeroelastic and aeroservoelastic behavior during flight. Tuning the FE model using measured data has been a challenging problem in structural dynamics for more than five decades. There has been great effort in the past couple of decades in developing methods to update these FE models to match computed frequencies and mode shapes to the measured GVT data [1–5]. An FE model tuning tool using GVT data has also been developed at the NASA Armstrong Flight Research Center (AFRC) [6–8] to minimize uncertainties in an analytical FE model. Most recent efforts to address this problem have focused on applying similar techniques to the health monitoring of structures [9–12]. Literature surveys on the FE model tuning are summarized in Refs. [13–15].

An FE model tuning of an aircraft is critical to having accurate aeroelastic and aeroservoelastic behavior during flight. When computed modes are not accurately correlated with measured GVT data, there can be significant and unknown inaccuracies in the results from

Presented at the AIAA SciTech Forum, National Harbor, MD, January 23–27, 2023; received 23 August 2022; revision received 9 December 2022; accepted for publication 31 December 2022; published online 30 January 2023.

*Subject Matter Expert in Analytical Structural Dynamics, Aerostructures Branch, P.O. Box 273, Mailstop 48202A.

dynamic load, flutter [7], or aeroservoelastic stability analyses. These errors can be caused by differences in mode shapes or modal frequencies; thus, the correlation procedures used to match the GVT data and computed modes should include both natural frequencies and mode shapes. The general perception is that any discrepancies between tests and analysis are due solely to modeling uncertainties. Errors in measured modal data are also associated with sensor reliability, sensor/actuator installation, supporting structures, measurement noise, curve fitting, or the experimentalist performing modal tests [15].

The primary objective of this study is to develop and validate a straightforward and efficient technique for inclusion of the measured test data into the FE model. Calculations of the objective function and constraints require a full FE analysis; this calculation process is time-consuming and expensive, especially when many iterations are required for optimization of a complex FE model. When using gradient-based optimization algorithms, using finite differences to calculate derivatives [6–8] makes the required computational time even longer. Presented in this paper is a computational approach to model tuning that employs analytical sensitivities for error indices based on the MSC NASTRAN software (Hexagon, Stockholm, Sweden) [16] and in-house pre- and postprocessor programs. During each design cycle, the set of design variables and constraints is redefined to improve the efficiency of the proposed approach. Accordingly, the efficiency of the method is increased, which also provides an incremental framework that allows for a faster, less-computationally-expensive model tuning procedure.

II. Mathematical Backgrounds

The mathematical equations for performance indices and their corresponding analytical sensitivity values will be derived in this section. These performance indices and sensitivity values are computed using the MSC NASTRAN software [16] with in-house computer programs. The following properties will be used for the structural model tuning procedure:

1) Total weight
2) Center of gravity (CG) location
3) Mass moment of inertias (if test data are available)
4) Static deformation under multiple load cases
5) Frequencies
6) Orthonormalized mass matrix or auto-orthogonality matrix (AOM)
7) Mode shape matrix or cross-orthogonality matrix (COM)

Figure 1 shows the object-oriented optimization (O3) tool [17] and the analysis submodules for the FE model tuning. Communication between the O3 tool and analysis submodules are performed using the design variables, performance indices, and sensitivity values of performance indices. When the O3 tool is started, then design variable values are saved on an external ASCII file based on the selected optimizer algorithm. This design variable file should be copied using a script command because an external file for a running program, O3, cannot be shared with any other analysis submodules until the O3 program is terminated. Each analysis submodule will be executed using the series of script commands. After running all the submodules, performance indices and corresponding sensitivity values are saved on external ASCII files. These performance indices and sensitivity values are used to create objective and constraint function values inside the O3 program and complete one cycle of the optimization run. Submodules in Fig. 1 can be categorized as the preprocessor, the analyzer, and the postprocessor modules. The "update NASTRAN input" belongs to a preprocedure module. This study uses the MSC NASTRAN analysis with a single iteration of solution 200 (optimization), selected analyzer module, as shown in Fig. 1. The MSC NASTRAN calculates response function values and sensitivity values of response functions. The postprocessor modules compute performance indices and their sensitivity values.

A. Weight Module

Total weight W and weight sensitivity values with respect to a design variable x_k, $\partial W/\partial x_k$, are obtained using the NASTRAN software. The performance index for the total weight, J_1 [8], and corresponding sensitivity value $\partial J_1/\partial x_k$ are obtained using Eqs. (1) and (2):

$$i\text{th performance index } J_i = \left(\frac{F_i(x_k) - F_{ir}}{F_{ir}}\right)^2 \tag{1}$$

$$\text{Sensitivity value of } J_i \frac{\partial J_i}{\partial x_k} = 2\left(\frac{F_i(x_k) - F_{ir}}{F_{ir}}\right)\left(\frac{1}{F_{ir}}\right)\frac{\partial F_i(x_k)}{\partial x_k} \tag{2}$$

where F_{ir} is the measured weight W_G and $F_i(x_k)$ and $\partial F_i(x_k)/\partial x_k$ are W and $\partial W/\partial x_k$, respectively.

The six-by-six weight information with respect to the reference point "o" from the NASTRAN output is given in Eq. (3):

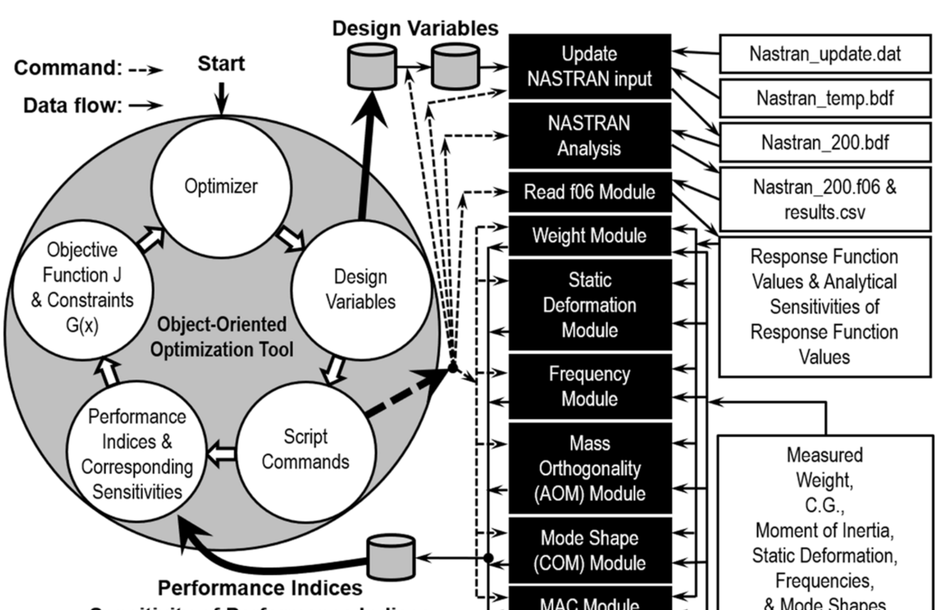

Fig. 1 Block diagram of analytical sensitivity-based structural model tuning tool.

$$[W] = \begin{bmatrix} W_{11} & W_{12} & W_{13} & W_{14} & W_{15} & W_{16} \\ W_{21} & W_{22} & W_{23} & W_{24} & W_{25} & W_{26} \\ W_{31} & W_{32} & W_{33} & W_{34} & W_{35} & W_{36} \\ W_{41} & W_{42} & W_{43} & W_{44} & W_{45} & W_{46} \\ W_{51} & W_{52} & W_{53} & W_{54} & W_{55} & W_{56} \\ W_{61} & W_{62} & W_{63} & W_{64} & W_{65} & W_{66} \end{bmatrix}$$

$$= \begin{bmatrix} W & 0 & 0 & 0 & Wz_{CG} & -Wy_{CG} \\ 0 & W & 0 & -Wz_{CG} & 0 & Wx_{CG} \\ 0 & 0 & W & Wy_{CG} & -Wx_{CG} & 0 \\ 0 & -Wz_{CG} & Wy_{CG} & I_{xxo} & I_{xyo} & I_{xzo} \\ Wz_{CG} & 0 & -Wx_{CG} & I_{yxo} & I_{yyo} & I_{yzo} \\ -Wy_{CG} & Wx_{CG} & 0 & I_{zxo} & I_{zyo} & I_{zzo} \end{bmatrix} \tag{3}$$

The CG location, therefore, can be obtained using Eq. (4):

$$x_{CG} = \frac{W_{26}}{W}$$
$$y_{CG} = \frac{W_{34}}{W}$$
$$z_{CG} = \frac{W_{15}}{W} \tag{4}$$

The response function values x_{CG}, y_{CG}, and z_{CG}, and corresponding sensitivity values $\partial x_{CG}/\partial x_k$, $\partial y_{CG}/\partial x_k$, and $\partial z_{CG}/\partial x_k$ are defined and computed using the NASTRAN solution 200 with bulk data entries DRESP1, DRESP2, and DEQATN [16]; therefore, performance indices J_i, $i = 2$, 3, and 4, and corresponding sensitivity values $\partial J_i/\partial x_k$ are also computed using Eqs. (1) and (2) as well as x_{CG}, y_{CG}, z_{CG}, $\partial x_{CG}/\partial x_k$, $\partial y_{CG}/\partial x_k$, and $\partial z_{CG}/\partial x_k$. The measured CG locations x_{MCG}, y_{MCG}, and z_{MCG} are the reference values F_{2r}, F_{3r}, and F_{4r} in this computation.

The diagonal terms of the mass moment of inertia matrix with respect to the CG location are computed using Eqs. (5–7):

$$I_{xxG} = I_{xxo} - W(y_{CG}^2 + z_{CG}^2) = W_{44} - W(y_{CG}^2 + z_{CG}^2) \tag{5}$$

$$I_{yyG} = I_{yyo} - W(z_{CG}^2 + x_{CG}^2) = W_{55} - W(z_{CG}^2 + x_{CG}^2) \tag{6}$$

$$I_{zzG} = I_{zzo} - W(x_{CG}^2 + y_{CG}^2) = W_{66} - W(x_{CG}^2 + y_{CG}^2) \tag{7}$$

Based on the NASTRAN compatible sign convention, the off-diagonal terms of the mass moment of inertia matrix are expressed in Eqs. (8–10):

$$I_{xyG} = I_{xyo} - W \times x_{CG} \times y_{CG} = -W_{45} - W \times x_{CG} \times y_{CG} \tag{8}$$

$$I_{yzG} = I_{yzo} - W \times y_{CG} \times z_{CG} = -W_{56} - W \times y_{CG} \times z_{CG} \tag{9}$$

$$I_{zxG} = I_{zxo} - W \times z_{CG} \times x_{CG} = -W_{64} - W \times z_{CG} \times x_{CG} \tag{10}$$

Performance indices J_i, $i = 5, \ldots,$ and 10, and corresponding sensitivity values, $\partial J_i/\partial x_k$, for mass moment of inertias can also be obtained using Eqs. (1) and (2) together with the NASTRAN computed response function values I_{xxG}, I_{yyG}, I_{zzG}, I_{xyG}, I_{yzG}, and I_{zxG}; corresponding sensitivity values $\partial I_{xxG}/\partial x_k$, $\partial I_{yyG}/\partial x_k$, $\partial I_{zzG}/\partial x_k$, $\partial I_{xyG}/\partial x_k$, $\partial I_{yzG}/\partial x_k$, and $\partial I_{zxG}/\partial x_k$; and the measured reference values I_{xxMG}, I_{yyMG}, I_{zzMG}, I_{xyMG}, I_{yzMG}, and I_{zxMG}.

B. Frequency Module

In this study, it is assumed that the m number of analytical frequencies f_j, $j = 1, 2, \ldots, m$, will be matched to the m-measured GVT frequencies f_{jG}, $j = 1, 2, \ldots, m$. Initially, these frequencies (response function values) f_j, $j = 1, 2, \ldots, m$, and corresponding sensitivity values $\partial f_j/\partial x_k$ are computed using the NASTRAN solution 200. Next, performance indices J_i, $i = 11, 12$, and $10 + m$, and corresponding sensitivity values, $\partial J_i/\partial x_k$, are computed using Eqs. (1) and (2). In this case, the reference values, F_{ir}, are the m measured GVT frequencies, f_{jG}, $j = 1, 2, \ldots, m$.

C. Orthogonality Module

The AOM and COM are computed using Eqs. (11) and (12), respectively [8]:

$$\boldsymbol{M}_{\mathrm{AOM}} = \boldsymbol{\Phi}_{GR}^T \boldsymbol{M}_R \boldsymbol{\Phi}_{GR} \quad (\text{order} = m \times m) \tag{11}$$

$$\boldsymbol{M}_{\mathrm{COM}} = \boldsymbol{\Phi}_{GR}^T \boldsymbol{M}_R \boldsymbol{\Phi}_{R} \quad (\text{order} = m \times m) \tag{12}$$

The detailed derivation of the system equivalent reduction expansion process (SEREP) [18] is given in Appendix A, where the order of a reduced-order mass matrix $\boldsymbol{M}_R$ in Eq. (13) is based on reduced degrees of freedom (DOF).

$$\boldsymbol{M}_R = \boldsymbol{\Psi}^{\boldsymbol{T}} \boldsymbol{\Psi} \quad (\text{order} = n_{RDOF} \times n_{RDOF}) \tag{13}$$

The matrix $\boldsymbol{\Psi}$ in Eq. (14) is used for the transformation matrix $\boldsymbol{T}$ of the SEREP, as shown in Eq. (15):

$$\boldsymbol{\Psi} = (\boldsymbol{\Phi}_R^T \boldsymbol{\Phi}_R)^{-1} \boldsymbol{\Phi}_R^T \quad (\text{order} = m \times n_{RDOF}) \tag{14}$$

$$\boldsymbol{T} = \boldsymbol{\Phi}\boldsymbol{\Psi} \quad (\text{order} = n_{FDOF} \times n_{RDOF}) \tag{15}$$

In Eq. (16), matrices $\boldsymbol{\Phi}_M$ (order $= n_{MDOF} \times m$) and $\boldsymbol{\Phi}_S$ (order $= (n_{RDOF} - n_{MDOF}) \times m$) are the master and slave eigenmatrices. From Eqs. (13) and (14), reduced-order mass matrix $\boldsymbol{M}_R$ and $\boldsymbol{\Phi}_R$ satisfy Eq. (17):

$$\boldsymbol{\Phi}_R \equiv \begin{bmatrix} \boldsymbol{\Phi}_M \\ \boldsymbol{\Phi}_S \end{bmatrix} \quad (\text{order} = n_{RDOF} \times m) \tag{16}$$

$$\boldsymbol{\Phi}_R^T \boldsymbol{M}_R \boldsymbol{\Phi}_R = \boldsymbol{I} \quad (\text{order} = m \times m) \tag{17}$$

The matrix $\tilde{\boldsymbol{\Phi}}_{GM}$ (order $= n_{MDOF} \times m$) in Eq. (18) is the measured eigenmatrix obtained from the GVT. The row DOF n_{MDOF} should be expanded to the reduced DOF n_{RDOF} to perform the matrix triple-multiplications in Eqs. (11) and (12). An expanded eigenmatrix $\boldsymbol{\Phi}_{GR}$ is also computed using SEREP, as shown in Eq. (18). The matrix $\boldsymbol{\Psi}_M$ in Eq. (18) is given in Eq. (19):

$$\boldsymbol{\Phi}_{GR} = \begin{bmatrix} \boldsymbol{\Phi}_M \boldsymbol{\Psi}_M \\ \boldsymbol{\Phi}_S \boldsymbol{\Psi}_M \end{bmatrix} \tilde{\boldsymbol{\Phi}}_{GM} \quad (\text{order} = n_{RDOF} \times m) \tag{18}$$

$$\boldsymbol{\Psi}_M = (\boldsymbol{\Phi}_M^T \boldsymbol{\Phi}_M)^{-1} \boldsymbol{\Phi}_M^T \quad (\text{order} = m \times n_{MDOF}) \tag{19}$$

In this study, this expanded eigenmatrix $\boldsymbol{\Phi}_{GR}$ is normalized with respect to the reduced-order mass matrix $\boldsymbol{M}_R$ once at the start of the design configuration, and then it will be assumed that $\boldsymbol{\Phi}_{GR}$ is constant during the optimization cycle. The numbers n_{RDOF} and n_{MDOF} are the number of the reduced DOF and the number of the master (or measured) DOF, respectively. Performance of the FE model tuning procedure and the quality of the expanded eigenmatrix $\boldsymbol{\Phi}_{GR}$ are related to the accelerometer locations [19] and the selection of the reduced-order model.

Diagonal and off-diagonal terms of matrices $\boldsymbol{M}_{\mathrm{AOM}}$ and $\boldsymbol{M}_{\mathrm{COM}}$ are selected as performance indices. First, a response function value $\boldsymbol{\Phi}_R$ (reduced-order eigenmatrix) and corresponding sensitivity matrix $\partial \boldsymbol{\Phi}_R/\partial x_k$ are obtained from the NASTRAN software.

The sensitivity matrices $\partial \boldsymbol{M}_{\mathrm{AOM}}/\partial x_k$ and $\partial \boldsymbol{M}_{\mathrm{COM}}/\partial x_k$ from Eqs. (11) and (12) become Eqs. (20) and (21), respectively:

$$\frac{\partial \boldsymbol{M}_{\mathrm{AOM}}}{\partial x_k} = \frac{\partial \boldsymbol{\Phi}_{GR}^T \boldsymbol{M}_R \boldsymbol{\Phi}_{GR}}{\partial x_k} = \boldsymbol{\Phi}_{GR}^T \frac{\partial \boldsymbol{M}_R}{\partial x_k} \boldsymbol{\Phi}_{GR} \tag{20}$$

$$\frac{\partial \boldsymbol{M}_{\mathrm{COM}}}{\partial x_k} = \frac{\partial \boldsymbol{\Phi}_{GR}^T \boldsymbol{M}_R \boldsymbol{\Phi}_{R}}{\partial x_k} = \boldsymbol{\Phi}_{GR}^T \frac{\partial \boldsymbol{M}_R}{\partial x_k} \boldsymbol{\Phi}_{R} + \boldsymbol{\Phi}_{GR}^T \boldsymbol{M}_R \frac{\partial \boldsymbol{\Phi}_R}{\partial x_k} \tag{21}$$

The sensitivity matrix $\partial \boldsymbol{\Phi}_R/\partial x_k$ in Eq. (21) is directly obtained from the NASTRAN computation as mentioned before; therefore, $\partial \boldsymbol{M}_R/\partial x_k$ should be computed to have $\partial \boldsymbol{M}_{\mathrm{AOM}}/\partial x_k$ and $\partial \boldsymbol{M}_{\mathrm{COM}}/\partial x_k$ values. First, $\partial \boldsymbol{M}_R/\partial x_k$ in Eqs. (20) and (21) is derived as in Eq. (22) using Eq. (13):

$$\frac{\partial \boldsymbol{M}_R}{\partial x_k} = \frac{\partial \boldsymbol{\Psi}^T}{\partial x_k} (\boldsymbol{\Phi}_R^T \boldsymbol{\Phi}_R)^{-1} \boldsymbol{\Phi}_R^T + \boldsymbol{\Phi}_R (\boldsymbol{\Phi}_R^T \boldsymbol{\Phi}_R)^{-T} \frac{\partial \boldsymbol{\Psi}}{\partial x_k} \tag{22}$$

The sensitivity of $\boldsymbol{\Psi}$ in Eq. (14) is derived as in Eq. (23). The details are given in Appendix B:

$$\frac{\partial \boldsymbol{\Psi}}{\partial x_k} = (\boldsymbol{\Phi}_R^T \boldsymbol{\Phi}_R)^{-1} \frac{\partial \boldsymbol{\Phi}_R^T}{\partial x_k} - (\boldsymbol{\Phi}_R^T \boldsymbol{\Phi}_R)^{-1} \left(\frac{\partial \boldsymbol{\Phi}_R^T}{\partial x_k} \boldsymbol{\Phi}_R + \boldsymbol{\Phi}_R^T \frac{\partial \boldsymbol{\Phi}_R}{\partial x_k} \right) (\boldsymbol{\Phi}_R^T \boldsymbol{\Phi}_R)^{-1} \boldsymbol{\Phi}_R^T \tag{23}$$

therefore, the matrix $\partial \boldsymbol{M}_R/\partial x_k$ in Eqs. (20) and (21) becomes Eq. (24):

$$\begin{aligned} \frac{\partial \boldsymbol{M}_R}{\partial x_k} = {} & \left[(\boldsymbol{\Phi}_R^T \boldsymbol{\Phi}_R)^{-1} \frac{\partial \boldsymbol{\Phi}_R^T}{\partial x_k} - (\boldsymbol{\Phi}_R^T \boldsymbol{\Phi}_R)^{-1} \left(\frac{\partial \boldsymbol{\Phi}_R^T}{\partial x_k} \boldsymbol{\Phi}_R \right.\right. \\ & \left.\left. + \boldsymbol{\Phi}_R^T \frac{\partial \boldsymbol{\Phi}_R}{\partial x_k} \right) (\boldsymbol{\Phi}_R^T \boldsymbol{\Phi}_R)^{-1} \boldsymbol{\Phi}_R^T \right]^T (\boldsymbol{\Phi}_R^T \boldsymbol{\Phi}_R)^{-1} \boldsymbol{\Phi}_R^T \\ & + \boldsymbol{\Phi}_R (\boldsymbol{\Phi}_R^T \boldsymbol{\Phi}_R)^{-T} \left[(\boldsymbol{\Phi}_R^T \boldsymbol{\Phi}_R)^{-1} \frac{\partial \boldsymbol{\Phi}_R^T}{\partial x_k} - (\boldsymbol{\Phi}_R^T \boldsymbol{\Phi}_R)^{-1} \left(\frac{\partial \boldsymbol{\Phi}_R^T}{\partial x_k} \boldsymbol{\Phi}_R \right.\right. \\ & \left.\left. + \boldsymbol{\Phi}_R^T \frac{\partial \boldsymbol{\Phi}_R}{\partial x_k} \right) (\boldsymbol{\Phi}_R^T \boldsymbol{\Phi}_R)^{-1} \boldsymbol{\Phi}_R^T \right] \end{aligned} \tag{24}$$

The performance indices J_{ij}, for each off-diagonal element of the AOM and COM in Eqs. (11) and (12), respectively, and corresponding sensitivity value $\partial J_{ij}/\partial x_k$ are obtained using Eqs. (25) and (26):

$$J_{ij} \equiv m_{ij}^2 \tag{25}$$

$$\frac{\partial J_{ij}}{\partial x_k} = 2 m_{ij} \frac{\partial m_{ij}}{\partial x_k} \tag{26}$$

where an off-diagonal term m_{ij} is the ith-row and jth-column element of the AOM ($\boldsymbol{M}_{\mathrm{AOM}}$), or COM ($\boldsymbol{M}_{\mathrm{COM}}$). Similarly, $\partial m_{ij}/\partial x_k$ is the ith-row and jth-column element of $\partial \boldsymbol{M}_{\mathrm{AOM}}/\partial x_k$ or $\partial \boldsymbol{M}_{\mathrm{COM}}/\partial x_k$.

The performance indices J_{ii} for each diagonal element of the COM in Eq. (12) and corresponding sensitivity value $\partial J_{ii}/\partial x_k$ are obtained using Eqs. (27) and (28):

$$J_{ii} \equiv 1 - m_{ii}^2 \tag{27}$$

$$\frac{\partial J_{ii}}{\partial x_k} = -2 m_{ii} \frac{\partial m_{ii}}{\partial x_k} \tag{28}$$

D. Static Deformation Module

A static deformation and corresponding sensitivity values are also computed using the NASTRAN software. The performance index J_{Li} for the ith load case and corresponding sensitivity value with respect to a design variable x_k, $\partial J_{Li}/\partial x_k$, are obtained using Eqs. (29) and (30):

$$\text{Performance index for the } i\text{th load case } J_{Li} = \frac{1}{m_p} \sum_{j=1}^{m_p} (\Delta_{ij} - \Delta_{ijT})^2 \tag{29}$$

$$\text{Sensitivity value of } J_{Li} \; \frac{\partial J_{Li}}{\partial x_k} = \frac{1}{m_p} \sum_{j=1}^{m_p} 2(\Delta_{ij} - \Delta_{ijT}) \frac{\partial \Delta_{ij}}{\partial x_k} \tag{30}$$

where Δ_{ijT} and Δ_{ij} are the measured and corresponding analytical deformations at the jth deformation sensor under the ith load condition, respectively, and m_p is the total number of deformation sensors during static tests such as proof and calibration tests. The deformation values Δ_{ij} and corresponding sensitivity values $\partial \Delta_{ij}/\partial x_k$ are obtained using the NASTRAN solution 200.

III. Numerical Validation of New Structural Model Tuning Tool

This section validates the structural model tuning tool with analytical sensitivity values. The example problem is based on a cantilevered Aerostructures Test Wing (ATW) 4 model.

A. Structural Dynamic Model Tuning of the Cantilevered Aerostructures Test Wing 4 Model

1. Correlation of the Baseline Aerostructures Test Wing 4 Model with Respect to Ground Vibration Test Data

The two variants of the ATW4, baseline and curvilinear spars and ribs (SpaRibs) [20], have been manufactured under two NASA Small Business Technology Transfer (STTR; contract numbers: NNX14 CD16P and NNX15CD08C). In this study, the baseline ATW4 is chosen as an example. The GVT has been performed to validate the FE model of the baseline ATW4. The grid numbers with accelerometer direction and geometric locations are given in Table 1 and Fig. 2a. The PCB® (PCB Piezotronics, Inc., Depew, NY) tri-axial and miniature teardrop accelerometers are used on the mounting table and test article, respectively, as shown in Figs. 2b and 2c. Figure 2b shows that two tri-axial accelerometers are used to monitor the movement of the mounting table. Impulse testing with the PCB® 086C02 impulse hammer (Figs. 2c and 2d) has been performed. The out-of-plane (Z-direction) excitation is hit right next to the accelerometer position 3, as shown in Figs. 2a and 2c. On the other hand, position 11 in Figs. 2a and 2d is hit for the in-plane (X-direction) excitation.

The first five measured frequencies, except mode 4, are given in the top half section of Table 2, third column. Measured weight and X- and Y-CG positions, without the aluminum L bracket, are also provided in Table 2. Natural frequencies of the baseline ATW4 model in Fig. 3a are given in the top half section of Table 2, fourth and fifth columns. Corresponding AOM and COM that were obtained from the GVT correlation study are provided in Table 3. An unsteady aerodynamic model with spline points for the flutter analysis using the ZAERO (ZONA Technology, Inc., Scottsdale, AZ) software [21] is also given in Fig. 3b. The flutter speed and frequency of the baseline ATW4 at Mach 0.75 are shown in Table 4, second column. Modal participation factors for the primary flutter mode at Mach 0.75 are shown in Table 2, second column. The most important modes for the primary flutter mode are the modes (1, 2, 3, and 5), as shown in Table 2. These four modes cover 100% of the primary flutter mode; therefore, these four modes are selected as the primary modes for model tuning. Figures 4a and 4b show the velocity versus structural damping (V–g) and velocity versus frequency (V–f) curves obtained from the flutter analysis before model tuning. Large amount of frequency errors (noted in Table 2) for the primary modes 17.8, 13.5, and 7.38% are observed with the baseline ATW4 configuration; all of the off-diagonal terms of the AOM (except the third-row and first-column element) and half of the off-diagonal terms of the COM violate 10% military and NASA requirements. Because all of the diagonal terms of the COM violate the 90% requirement, structural dynamic model tuning is required to have a reliable flutter boundary.

Table 1 Geometric locations of accelerometers

Accelerometer no.	Grid no. with (DOF)	*X* coordinate, in.	*Y* coordinate, in.	*Z* coordinate, in.
1	1847 (*Z*)	9.93	7.20	0.19
2	2315 (*Z*)	13.58	10.8	0.17
3	1484 (*Z*)	17.22	14.4	0.16
4	1370 (*Z*)	15.14	3.60	0.03
5	2232 (*Z*)	18.06	7.20	0.03
6	2606 (*Z*)	20.99	10.8	0.03
7	1754 (*Z*)	23.92	14.4	0.03
8	2 (*Z*)	12.75	18.5	0
9	31 (*Z*)	32.83	18.5	0
10	2 (*X*)	12.75	18.5	0
11	31 (*X*)	32.83	18.5	0

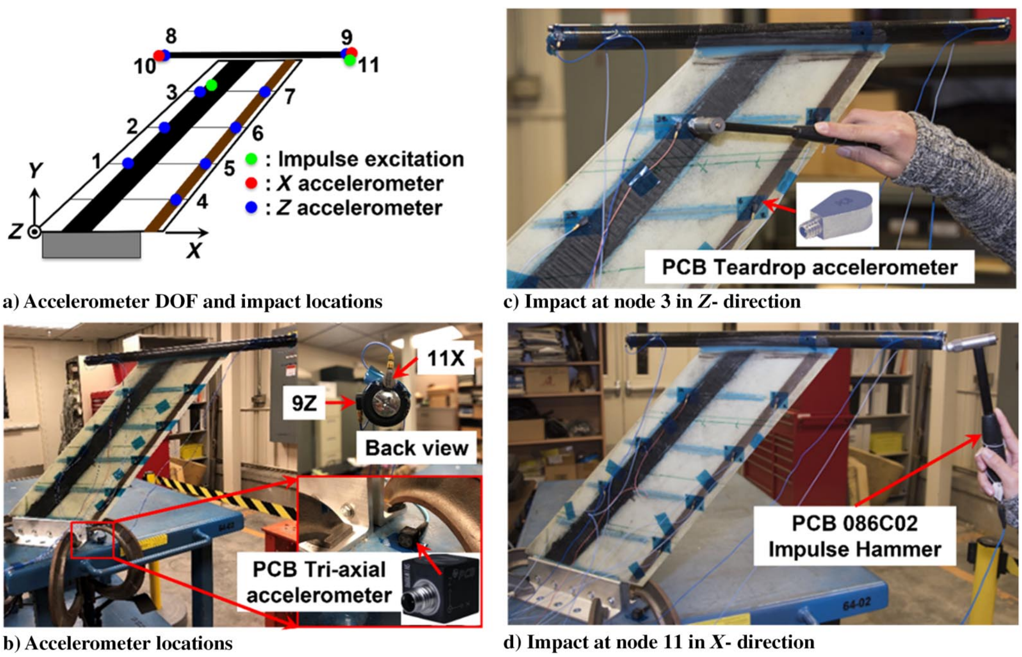

a) Accelerometer DOF and impact locations
c) Impact at node 3 in *Z*- direction
b) Accelerometer locations
d) Impact at node 11 in *X*- direction

Fig. 2 Ground vibration test of the baseline Aerostructures Test Wing 4.

Table 2 Weight, center of gravity, and natural frequencies of example problem

			Baseline model		Delivered model		Fixed model	
Parameter	MPF	GVT	FEM	% Error	FEM	% Error	FEM	% Error
Weight (lb)		1.686	1.742	3.33	1.742	3.33	1.744	3.43
X-CG (in.)	**N/A**	13.37	13.67	2.24	13.67	2.24	13.64	2.01
Y-CG (in.)		7.763	7.944	2.33	7.944	2.33	7.934	2.20
Mode 1 (Hz)	**5.37%**	**14.65**	**17.26**	**17.8**	**14.62**	**−0.17**	**15.17**	**3.55**
Mode 2 (Hz)	**93.5%**	**29.55**	**33.54**	**13.5**	**29.15**	**−1.36**	**30.08**	**1.79**
Mode 3 (Hz)	**0.87%**	**84.92**	**91.18**	**7.38**	**77.37**	**−8.89**	**81.01**	**−4.60**
Mode 5 (Hz)	**0.27%**	**181.8**	**184.5**	**1.47**	**158.9**	**−12.6**	**175.3**	**−3.58**
Mode 6 (Hz)	0.00%	210.7	228.0	8.21	194.0	−7.92	198.8	−5.65

	After iteration 1		After iteration 2		After iteration 3		After iteration 4	
Parameter	FEM	% Error	FEM	% Error	FEM	% Error	FEM	% Error
Weight (lb)	**1.686**	0.00	1.721	2.05	1.726	2.39	1.706	1.17
X-CG (in.)	13.55	1.32	13.71	2.51	13.79	3.17	13.64	2.04
Y-CG (in.)	7.825	0.80	8.008	3.16	8.159	5.10	**7.986**	2.87
Mode 1 (Hz)	**15.57**	**6.34**	**15.07**	**2.91**	**14.73**	**0.57**	**15.11**	**3.16**
Mode 2 (Hz)	**30.68**	**3.79**	**29.91**	**1.21**	**29.20**	**−1.21**	**29.82**	**0.88**
Mode 3 (Hz)	**82.44**	**−2.93**	**81.71**	**−3.79**	**82.63**	**−2.69**	**82.94**	**−2.34**
Mode 5 (Hz)	**178.3**	**−1.90**	**177.8**	**−2.16**	**179.1**	**−1.50**	**178.8**	**−1.64**
Mode 6 (Hz)	203.0	−3.69	202.4	−3.95	205.4	−2.52	205.2	−2.62

MPF, modal participation factor; GVT, ground vibration test; FEM, finite element model.
Black shading: objective function.
Gray shading: violated 3–5% requirement, active constraint, or too much error (for weight and CG locations).
Boldfaced numbers: primary modes or objective function values.

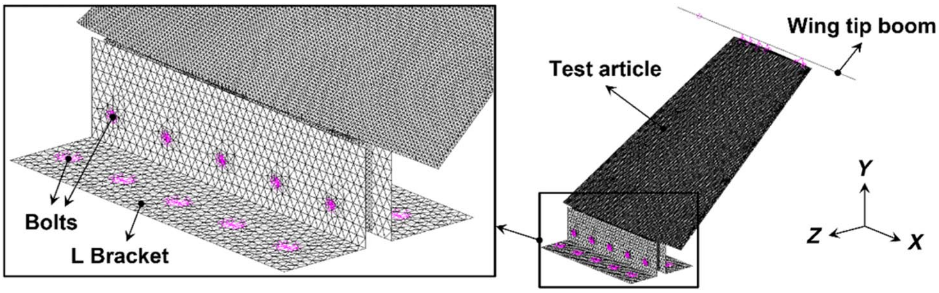

a) Finite element structural dynamic model

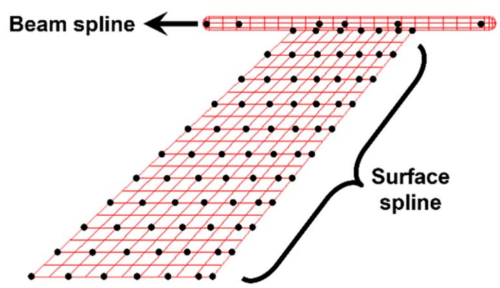

b) Aerodynamic model

Fig. 3 Structural and aerodynamic models of Aerostructures Test Wing 4.

Table 3 Auto- and cross-orthogonality matrices using baseline model

	Auto-orthogonality matrix						Cross-orthogonality matrix				
Mode	1	2	3	5	6	Mode	1	2	3	5	6
1	1.000	−0.431	−0.019	−0.110	0.143	1	−0.867	−0.287	0.007	0.038	0.016
2	−0.431	1.000	−0.491	0.775	0.382	2	−0.046	0.798	0.046	−0.080	0.003
3	−0.019	−0.491	1.000	−0.565	−0.405	3	0.218	−0.480	−0.842	0.055	−0.041
5	−0.110	0.775	−0.565	1.000	0.477	5	−0.226	0.773	0.111	−0.534	0.158
6	0.143	0.382	−0.405	0.477	1.000	6	−0.300	0.453	0.1--14	0.161	0.816

Gray shading: violated 10% (off-diagonal terms) and 90% (diagonal terms of COM) requirement.

Table 4 Flutter boundaries of Aerostructures Test Wing 4 models

		Delivered model		Fixed model		After iteration 4	
Flutter boundary	Baseline model	Value	% Difference	Value	% Difference	Value	% Difference
Speed (KEAS)	196.40	172.63	−12.1	177.43	−9.66	178.89	−8.91
Frequency (Hz)	29.92	25.85	−13.6	26.85	−10.3	25.93	−13.3

KEAS, knots equivalent air speed.

2. Correlation of the Delivered Model

The STTR project team provided a tuned model, the "delivered model." This ATW4 FE model has uncertainties associated with the composite manufacturing process and the FE idealization used in the delivered model, which was already tuned by the contractor [20]. The five natural frequencies, modes (1, 2, 3, 5, and 6), of the delivered model are given in the top half section of Table 2, sixth and seventh columns. The first two modes meet military and NASA requirements. The frequency errors for the third and fourth primary modes, however, violate the standards, and the frequency errors for the fifth mode (mode 6) is relatively large. The corresponding AOM and COM are given in Table 5. One off-diagonal term of the COM for the primary mode, 10.7%, violates "10% requirements" in military and NASA standards. This violation is negligibly small compared to the frequency violations.

Flutter analysis is performed using the delivered model, and the flutter speed and frequency are shown in Table 4, third and fourth columns. The flutter speed and frequency differences are 12.1 and 13.6%, respectively. A large improvement in the first two frequencies, AOM, and COM results in more than 12% flutter speed and frequency changes.

A composite test article is mounted on the ground using aluminum L brackets and bolts, as shown in Fig. 3a. In the delivered model, these bolts are idealized as rigid and uniform beam elements (RBE2 and CBAR in NASTRAN terminology). As a result, the delivered FE model allows small relative motion between the L brackets and the test article and the ground. The third and fourth mode shapes from the back view are prepared in Fig. 5. Because of the relative motions shown in Figs. 5a and 5b, the corresponding frequencies are more flexible than the measured frequencies with large prediction errors, 8.89 and 12.6%.

In this study, the FE model with the additional constraints at the L bracket (Fig. 6) will be called the "fixed model." The first five flexible modes, except the in-plane motion (mode 4) from the fixed model are also summarized in the top half section of Table 2, eighth and ninth columns. Figures 5c and 5d show the third and fourth mode shapes from the back view. Relative deformations in Figs. 5a and 5b are suppressed using the additional rigid elements in Fig. 6.

When the idealization error is fixed, the frequency correlations are significantly improved, as shown in Table 2. Mode 2 satisfies the military and NASA standards; moreover, the first, third, and fourth primary modes also satisfy the NASA standard. The frequency error for the secondary mode is also less than 10%. The AOM and COM are listed in Table 6. Off-diagonal terms of the AOM and COM, 11 and 13%, violate the 10% requirement for primary modes.

Flutter analysis is also performed after fixing the idealization error, and the flutter speed and frequency results are given in Table 4, fifth

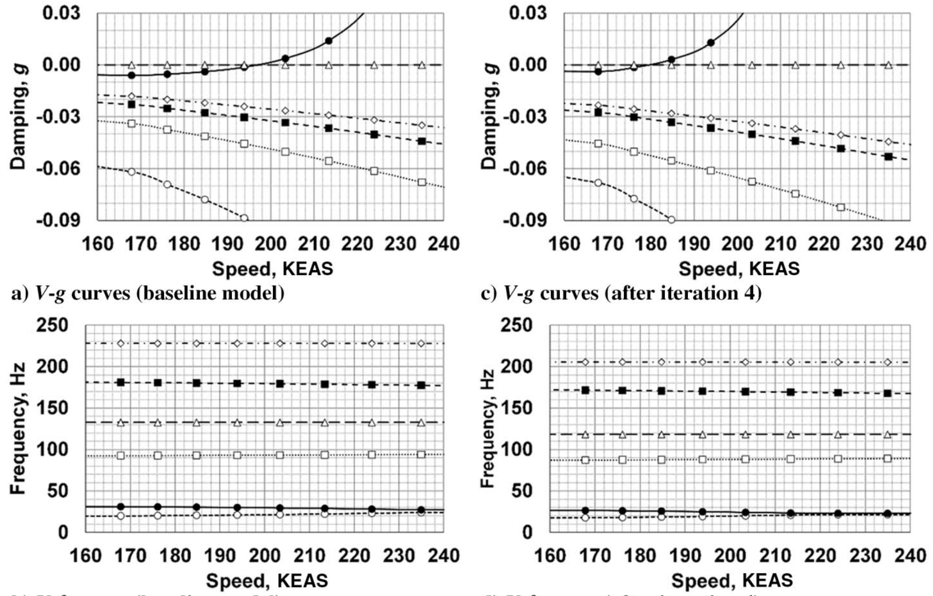

a) *V-g* curves (baseline model)
c) *V-g* curves (after iteration 4)
b) *V-f* curves (baseline model)
d) *V-f* curves (after iteration 4)

Fig. 4 ***V–g* and *V–f* curves at Mach 0.75 before and after model tuning. KEAS, knots equivalent air speed.**

Table 5 Auto- and cross-orthogonality matrices using delivered model

	Auto-orthogonality matrix						Cross-orthogonality matrix				
Mode	1	2	3	5	6	Mode	1	2	3	5	6
1	1.000	0.042	0.049	0.072	0.004	1	0.998	0.064	−0.024	−0.014	−0.003
2	0.042	1.000	−0.036	0.008	0.039	2	0.107	−0.993	0.034	0.030	−0.001
3	0.049	−0.036	1.000	0.093	0.007	3	0.024	0.004	−0.999	−0.022	0.005
5	0.072	0.008	0.093	1.000	0.031	5	0.061	−0.032	−0.070	−0.933	0.347
6	0.004	0.039	0.007	0.031	1.000	6	0.013	−0.029	−0.009	0.321	0.946

Gray shading: violated 10% requirement.

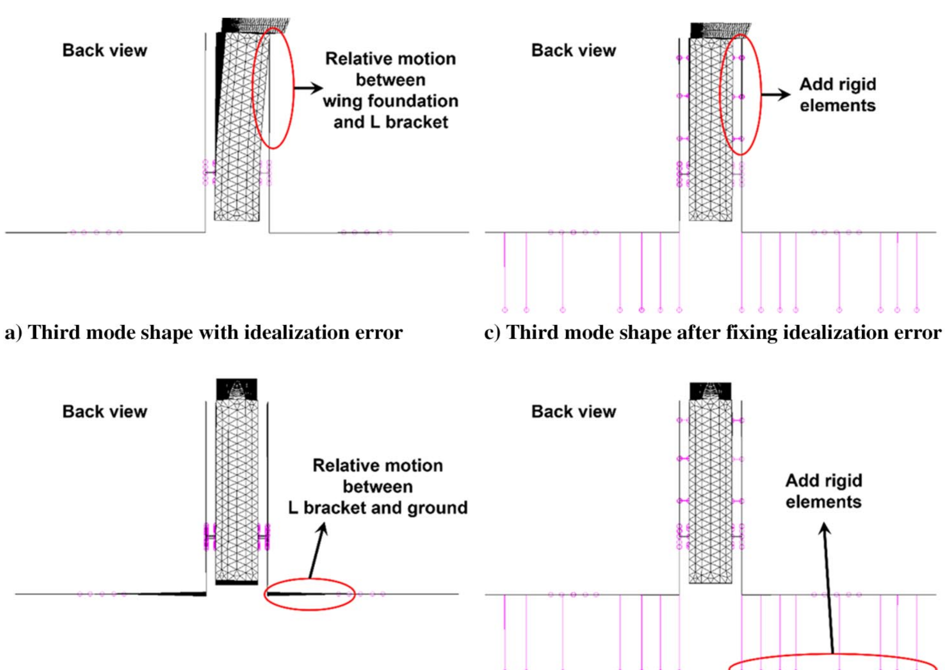

a) Third mode shape with idealization error
c) Third mode shape after fixing idealization error
b) Fourth mode shape with idealization error
d) Fourth mode shape after fixing idealization error

Fig. 5 Relative motion between L bracket and test article/ground.

and sixth columns. Flutter speed improved more than 2.4% by correcting boundary condition problems with the delivered model. It should be noted that the idealization error cannot be improved with a model tuning procedure.

3. *First Optimization Run*

A total of 797 candidate design variables, as listed in Table 7, are prepared in this study. These input cards for 797 design variables (DESVAR [16]) and design variable and model relations (such as

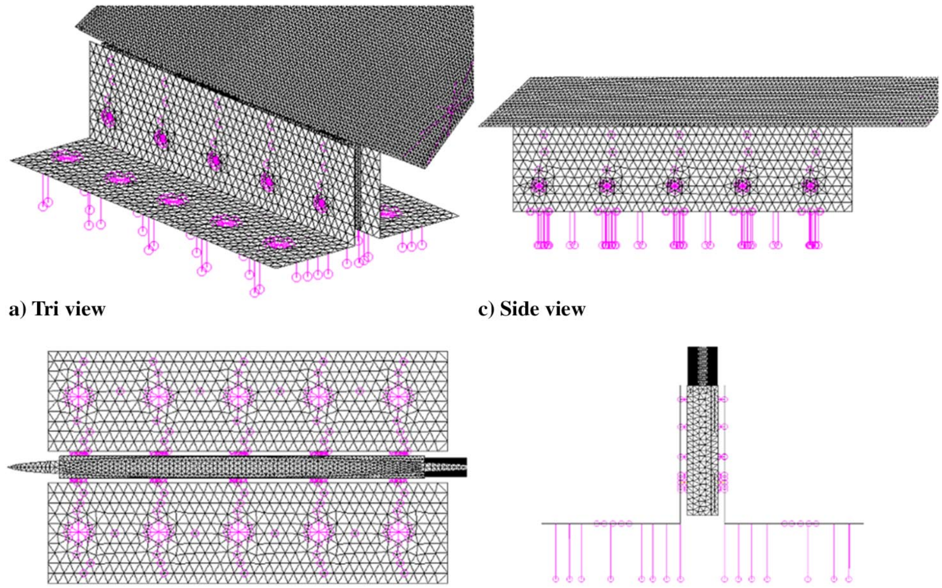

Fig. 6 Additional constraints to minimize relative motion between L bracket and test article/ground.

Table 6 Auto- and cross-orthogonality matrices using a fixed model

	Auto-orthogonality matrix						Cross-orthogonality matrix				
Mode	1	2	3	5	6	Mode	1	2	3	5	6
1	1.000	0.042	0.049	0.075	0.004	1	0.999	0.026	0.039	0.004	0.000
2	0.042	1.000	−0.037	0.020	0.032	2	0.069	−0.997	−0.011	−0.045	0.000
3	0.049	−0.037	1.000	0.110	−0.014	3	0.009	0.028	0.999	−0.028	0.023
5	0.075	0.020	0.110	1.000	0.080	5	0.067	−0.059	0.130	0.932	0.328
6	0.004	0.032	−0.014	0.080	1.000	6	0.007	−0.020	−0.042	−0.250	0.967

Gray shading: violated 10% requirement.

Table 7 Design variables selected during optimization iterations

Candidate DV nos.	Property [16]	Iteration 1	Iteration 2	Iteration 3	Iteration 4
1–15	MAT1	3	3	3	3
16–31	MAT8	2	2	2	2
32–34	PBARL	2	2	2	2
35	PSHELL	— —	— —	— —	— —
36–120	CONM2	— —	7	47	47
121–153	PELAS	— —	— —	— —	— —
154–475	PCOMP (thickness)	18	50	80	80
476–797	PCOMP (ply angle)	— —	— —	— —	— —
Total no. of design variables		25	64	134	134
Total no. of iterations		24	48	62	29

DV: design variable; MAT1: the material properties for linear isotropic materials; MAT8: the material properties for an orthotropic material for isoparametric shell elements; PBARL: the properties of a simple beam element by cross-sectional dimensions; PSHELL: the membrane: bending: transverse shear: and coupling properties of thin shell elements; CONM2: a concentrated mass element at a grid point; PELAS: the stiffness: damping coefficient: and stress coefficient of a scalar elastic (spring) elements; PCOMP: the properties of an n-ply composite material laminate.

DVMREL, DVPREL, and DVCREL [16]) must be included in the input deck of the NASTRAN solution 200. Once the sensitivity values of the response functions are obtained, the sensitivity values of the performance indices are computed using the in-house post-processing programs shown in Fig. 1. Absolute values of the objective sensitivity are sorted to select the most efficient design variables for optimizing the objective function value selected among performance indices.

An FE model tuning is not an easy task; therefore, we should improve the FE model gradually. If we start optimization in an infeasible domain [22], there is no guarantee that we can improve the model. Therefore, the unconstraint optimization is selected for the first optimization iteration to guarantee the feasible design. The total weight difference is nominated as an objective function value for the first optimization run without any constraint functions. A total of 25 of the most sensitive design variables in Table 7 are selected for the first optimization run. The design variables for the first optimization run are the densities of material properties, the diameters of the wing-tip boom, and the composite plate thicknesses.

After the first optimization, a total weight of 1.744 lb becomes the target value 1.686 lb, as shown in bottom half of Table 2, second and third columns; however, the first and second frequency errors of 3.55 and 1.79% become 6.34 and 3.79%, respectively. It should be noted in Table 2 that the X- and Y-CG location errors after the first optimization run are 1.32 and 0.80%, respectively, and these values are less than the 1.5% error.

4. Second Optimization Run

The first frequency error is selected for the objective function of the second optimization run. In this case, total weight, X- and Y-CG locations, and frequency errors of the modes (2, 3, 5, and 6) are chosen as the inequality constraint functions. The maximum allowable errors for the weight and frequency-related constraints are 3 and 5%, respectively. Before starting the second optimization run, sensitivity analysis with 797 design variables is again performed to decide the most efficient design variables. An additional 39 design variables, for a total of 64 ($= 25 + 39$) are selected, as shown in Table 7, fourth column. The glue material used for bonding spars, ribs, and wing cover skins is not uniformly applied during the composite manufacturing process. Lumped mass properties (CONM2) for the glue material and balancing weight at the leading and trailing edges of the wing-tip boom are involved in the optimization run.

The bottom half of Table 2, fourth and fifth columns, shows that the first frequency error of 6.34% reduces to 2.91% after the second optimization run. It should be noted that the Y-CG location becomes an active constraint at 3.16%, and it may be concluded that the first frequency error cannot be improved anymore because of the active constraint. The frequency errors for modes (1, 2, and 5) are less than 3%. Similarly, frequency errors for modes (3 and 6) are less than 5%. Table 8 shows that one of the off-diagonal terms of the primary modes of the AOM and COM is 11.3 and 13.3%, which slightly exceeds the 10% requirement.

5. Third Optimization Run

The orthogonality of the AOM and COM is improved in this optimization run. The off-diagonal term of the AOM (11.3%) in Table 8 (fourth row [mode 5], third column) is selected as the objective function for the third optimization run. Based on the same sensitivity analysis procedure, 70 additional design variables are added, as shown in Table 7 (fifth column). In this optimization run, the total weight X- and Y-CG locations belong to the inequality constraints with a maximum allowable error of 5% (compared to 3% in the second optimization run) to start optimization in a feasible domain [22]. The maximum allowable frequency errors for modes (1, 2), (5, 3), and (6) are 3, 5, and 10%, respectively. All off-diagonal terms of the AOM and COM are chosen as inequality constraints with a maximum allowable error of 10%, except for the objective function; the fourth row (mode 5) and third column of the COM; the fifth row (mode 6) and fourth column (mode 5) elements of the COM; and the fourth row (mode 5) and fifth column (mode 6) elements of the COM. Based on the NASA standard, diagonal terms of the COM are also selected as inequality constraints. A minimum allowable error of 90% is used in the case of diagonal terms.

After the third optimization run, the objective function value becomes 7.6% (7.8% with normalization). The off-diagonal term for the third primary mode (13.3% in Table 8) also becomes less than 10 at 9.8% (9.9% with normalization), as shown in Table 9. It should be noted in Tables 8 and 9 that the diagonal terms of the AOM are not equal to one because of the constant assumption for the expanded eigenmatrix $\mathbf{\Phi}_{GR}$, as shown in Eq. (18). The bottom half of Table 2, sixth and seventh columns, shows that frequency errors are all improved and satisfy inequality constraints. The inequality constraint associated with the Y-CG location, however, becomes an active constraint of 5.1% (slightly violating the 5% allowable).

6. Fourth Optimization Run

The Y-CG location error is selected as the objective function for the final optimization run with the same design variables as in Table 7, sixth column. The same constraint functions used in the third optimization run are also used for the final optimization run. The objective function for the third optimization run becomes an additional constraint function (also including the fourth-row and third-column element of the COM) with a less than 10% limit.

All results after the final optimization run are summarized in the bottom half of Table 2, eighth and ninth columns, and Table 10. All weight-related errors, including total weight, and X- and Y-CG locations are less than 3%. The most important primary frequency error (the second mode) is less than 1%. Similarly, the frequency errors of the other three primary modes are less than 3.2%, and the frequency error of the secondary mode (mode 6) is less than 2.7%. The frequency errors of the first five out-of-plane modes are all less than 3.2%. After the final optimization run, the AOM is normalized; the AOM and COM are shown in Table 10. Table 10 shows that all of the off-diagonal terms of the AOM are less than 10%. Similarly, all of the off-diagonal terms of the COM for the primary modes are less than 10%. Off-diagonal terms of the COM for the secondary mode become 24.7 and 32.0%. Also of note, all diagonal terms of the COM are greater than 93.8%. The final FE model correlates well with the test data.

All of the design variables that change more than 5% after the final optimization run are summarized in Table 11. The largest design variable change is a 12.7% decrease in the inner diameter of the circular wing-tip boom. This wing-tip boom is made with composite material, and the inner diameter of the hollow cross-sectional shape contains many uncertainties.

Table 8 Auto- and cross-orthogonality matrices after iteration 2

	Auto-orthogonality matrix						**Cross-orthogonality matrix**				
Mode	1	2	3	5	6	Mode	1	2	3	5	6
1	1.062	0.042	0.039	0.074	−0.004	1	1.030	0.027	0.040	−0.004	0.000
2	0.042	1.051	−0.043	0.025	0.029	2	0.067	−1.022	−0.011	0.046	0.000
3	0.039	−0.043	1.016	0.113	−0.013	3	−0.002	0.033	1.006	0.029	0.024
5	0.074	0.025	0.113	1.005	0.079	5	0.065	−0.063	0.133	−0.934	0.326
6	−0.004	0.029	−0.013	0.079	1.002	6	0.000	−0.017	−0.043	0.249	0.969

Gray shading: violated 10% requirement.

Table 9 Auto- and cross-orthogonality matrices after iteration 3

	Auto-orthogonality matrix						**Cross-orthogonality matrix**				
Mode	1	2	3	5	6	Mode	1	2	3	5	6
1	1.038	0.045	−0.001	0.068	0.029	1	1.018	0.026	0.040	−0.004	0.000
2	0.045	1.044	−0.054	0.040	0.041	2	0.071	−1.018	−0.008	0.044	0.000
3	−0.001	−0.054	0.970	**0.076**	−0.033	3	−0.041	0.044	0.983	0.024	0.026
5	0.068	0.040	**0.076**	0.975	0.075	5	0.061	−0.076	0.098	−0.926	0.315
6	0.029	0.041	−0.033	0.075	0.957	6	0.032	−0.027	−0.062	0.239	0.946

Black shading: objective function.
Underline: not objective or constraint function.
Gray shading: secondary mode.

Table 10 Auto- and cross-orthogonality matrices after iteration 4

	Auto-orthogonality matrix						Cross-orthogonality matrix				
Mode	1	2	3	5	6	Mode	1	2	3	5	6
1	1.000	0.041	0.023	0.067	0.018	1	0.999	0.024	0.040	0.004	0.000
2	0.041	1.000	−0.044	0.030	0.036	2	0.066	−0.997	−0.009	−0.044	0.000
3	0.023	−0.044	1.000	0.081	−0.029	3	−0.017	0.035	0.999	−0.025	0.025
5	0.067	0.030	0.081	1.000	0.075	5	0.061	−0.069	0.099	0.938	0.320
6	0.018	0.036	−0.029	0.075	1.000	6	0.022	−0.023	−0.058	−0.247	0.967

Gray shading: secondary mode.

Flutter analysis is performed at the same Mach number again with the updated FE model to check the effect of the structural dynamic model tuning on the flutter boundary. After the final model tuning, the $V–g$ and $V–f$ curves are shown in Figs. 4c and 4d. Flutter speed and frequency are shown in Table 4, seventh and eighth columns. Flutter speed and frequency differences with respect to the baseline model are 8.91 and 13.3%, respectively. Roughly, 2.5% (= 12.1–9.66%) of this flutter speed difference is a result of fixing the idealization error in the wing-root boundary condition.

The total weight and frequencies of the fixed model in Table 2 are already in acceptable shape. The average frequency error of the primary modes is 3.25%. After the four optimization iterations, the average frequency error becomes 2.01%; therefore, frequencies and total weight are improved by 1.24 and 2.26%, respectively. In Table 4, the flutter speed improvement is 0.75% (= 9.66–8.91%); therefore, the 3% requirement (military standard) for the frequency correlation of the primary modes and the 10% (11 and 13% in Table 5 are in an acceptable range) requirements for the off-diagonal terms of the AOM and COM are accurate enough to have a good flutter speed.

It is difficult to satisfy all the modal correlation requirements of a large aircraft structure with idealization errors. Theoretically, uncertainties related to the structural sizing and material properties can be improved using the FE model tuning procedure. It should be emphasized that fixing the idealization errors associated with the rigid boundary conditions and/or structural connection mechanisms are critical to have successful completion of the FE model tuning procedure. An unsteady aerodynamic model should be also tuned with respect to flight test data to have good flutter boundaries [23].

Table 11 Design variables change more than 5%

DV no.	Property	% Change
34	Diameter	−12.7
60	CONM2	−7.27
65	CONM2	6.22
108	CONM2	−5.16
109	CONM2	−6.89
110	CONM2	−7.98
111	CONM2	−8.83
112	CONM2	−8.78
113	CONM2	−8.08
114	CONM2	−7.57
115	CONM2	−6.33
303	PCOMP	−6.17
304	PCOMP	−6.20
305	PCOMP	−6.17
306	PCOMP	−7.24
307	PCOMP	−7.23
308	PCOMP	−7.24
309	PCOMP	−5.19
310	PCOMP	−5.09
311	PCOMP	−5.20
371	PCOMP	−6.16
372	PCOMP	−6.20
373	PCOMP	−6.16
374	PCOMP	−7.24
375	PCOMP	−7.23
376	PCOMP	−7.24
377	PCOMP	−5.20
378	PCOMP	−5.10
379	PCOMP	−5.21

DV, design variable; CONM2, a concentrated mass element at a grid point; PCOMP, the properties of an n-ply composite material laminate.

B. Finite Element Model Tuning of the Aerostructures Test Wing 4 Using Simulated Static Test Data

1. *Finite Element Model for a Simulated Static Test*

The thicknesses of the aluminum L bracket (0.25 in.) and a single layer of a composite plate (0.005 in.) are changed by 5% (0.2375 and 0.00525 in.) to create a sample numerical test case. Structural deformations are computed at the deformation measurement points listed in Table 12. Two load cases are considered in this model tuning with static deformation data. In the first case, 1 lb of positive Z-direction load is applied at 1 inch, aft of the midchord of the wing-tip boom. On the other hand, 1 lb of negative Z-direction load is applied at the leading edge of the wing-tip boom in the second load case. Structural deformations under these two load cases are shown in Fig. 7.

2. *Model Tuning Using Static Deformation Data*

The objective function used in this test case is a linear combination of the performance indices for the first and second load cases given in Eq. (31). Sensitivity values of the corresponding objective function value are shown in Eq. (32):

$$\text{Objective function } J = J_{L1} + J_{L2} \tag{31}$$

$$\text{Sensitivity of objective function } \frac{\partial J}{\partial x_k} = \frac{\partial J_{L1}}{\partial x_k} + \frac{\partial J_{L2}}{\partial x_k} \tag{32}$$

where J_{Li}, $i = 1, 2$, are defined in Eq. (29).

The histories of two design variables during the optimization run are shown in Fig. 8. The initial starting values of design variables 1 and 2 are 0.25 and 0.005 in., respectively. Figures 8c and 8d show that the sensitivity values of the objective function with respect to design variables 1 and 2 at the start of the optimization run are 0.026 and −0.0063, respectively. At the end of the optimization run, these sensitivity values become 4.2E−06 and 5.0E−05; therefore, the Kuhn–Tucker condition [22] is satisfied with an unconstrained optimization problem. After the optimization run, the design variables 1 and 2 become 0.2375 and 0.00525 in., respectively, as shown in Figs. 8a and 8b, which are target values used to generate target wing

Table 12 Grid and degree-of-freedom information about deformation measurements

Deformation measurements no.	Grid no. with measured DOF
1	1847 (X)
2	2315 (Y)
3	1484 (Z)
4	1370 (Z)
5	2232 (X)
6	2606 (Y)
7	1754 (Z)

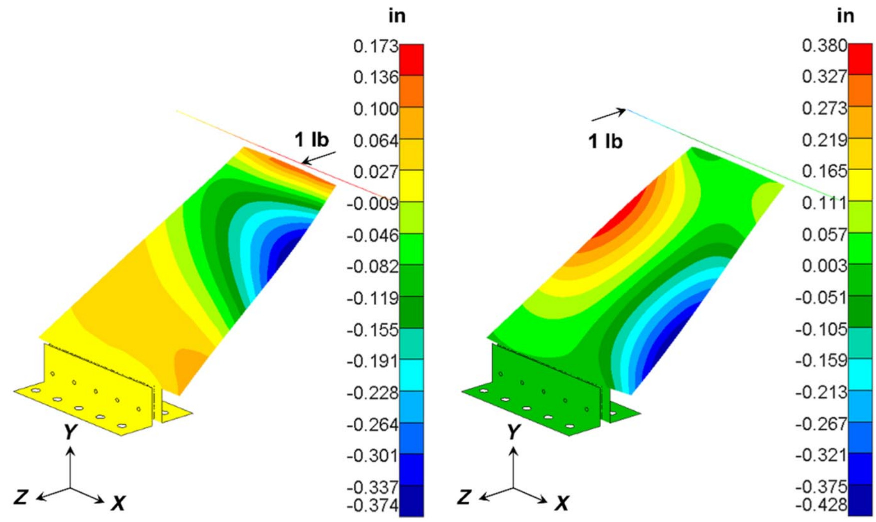

a) Z deformation under load case 1 b) Z deformation under load case 2

Fig. 7 Target deformation shapes under load cases 1 and 2.

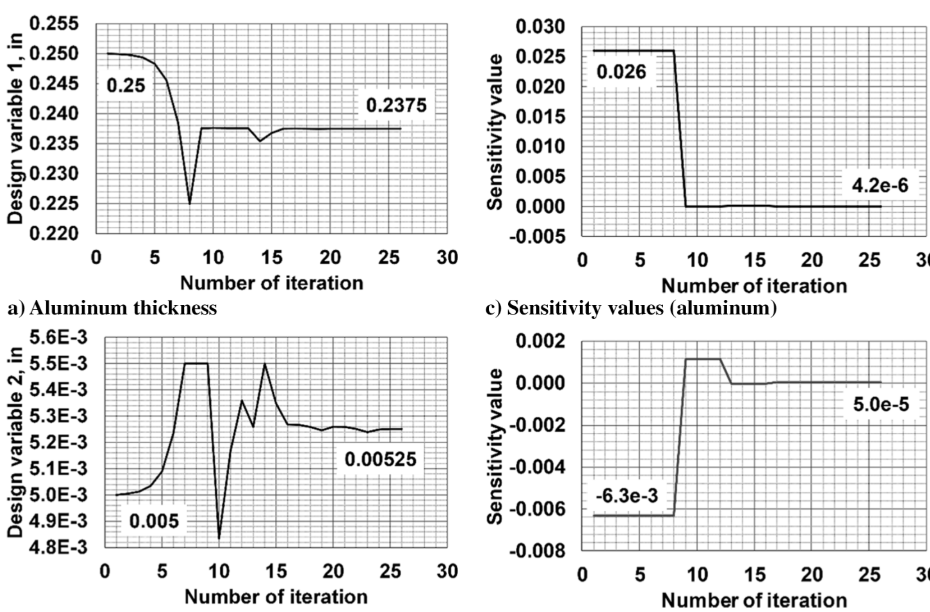

a) Aluminum thickness c) Sensitivity values (aluminum)

b) Composite layer thickness d) Sensitivity values (composite layer)

Fig. 8 Histories of design variables and design variable sensitivities during an optimization run.

deformations in Fig. 7. The performance of the static deformation module is demonstrated in this section.

IV. Conclusions

This study introduced a structural model tuning tool based on analytical sensitivity values that has been developed. Analytical sensitivity values of performance indices are computed using the NASTRAN-generated sensitivity values with the in-house computer programs.

All of the analysis modules for the new structural model tuning tool are tested using the Aerostructures Test Wing 4, which was developed at the NASA Armstrong Flight Research Center using NASA Small Business Technology Transfer Phase II, NNX15CD08C, for demonstrating flutter and advanced aeroelastic test techniques. Structural dynamic and static model tunings are performed separately using measured GVT data and computer simulated static data, respectively. The performance of the static deformation module has been demonstrated using the Aerostructures Test Wing 4 model.

After the structural dynamic model tuning, all of the weight-related errors, including total weight as well as X- and Y-CG locations, are less than 3%. The frequency errors of the first five out-of-plane modes are all less than 3.2%. All of the off-diagonal terms of the auto-orthogonality matrix are less than 10%. Similarly, all of the off-diagonal terms of the cross-orthogonality matrix for the primary modes are less than 10%. Off-diagonal terms of the cross-orthogonality matrix for the secondary modes become 24.7 and 32.0%. All of the diagonal terms of the cross-orthogonality matrix are greater than 93.8%.

The final FE model correlates well with the test data. The flutter speed decreases by 8.91% compared with the baseline Aerostructures Test Wing 4. Roughly, 2.5% of this flutter speed improvement is attributed to fixing the idealization error in the wing-root boundary condition. The 3% requirement for the frequency correlation of the primary modes with 10% requirements for the off-diagonal terms of the auto-orthogonality matrix and cross-orthogonality matrix is accurate enough to have a good flutter speed.

Appendix A: System Equivalent Reduction Expansion Process [18]

The governing equations of motion for an undamped structural system without any applied forces are written in Eq. (A1):

$$M\ddot{q} + Kq = 0 \tag{A1}$$

where M and K are the full-order mass and stiffness matrices, respectively, and $\ddot{q}$ and q are the acceleration and displacement vectors. The displacement vector q can be expressed using eigenmatrix Φ and the generalized coordinate η, as shown in Eq. (A2):

$$q = \Phi\eta \tag{A2}$$

Equations (A3) and (A4) show that the displacement vector q and the eigenmatrix Φ can be partitioned:

$$q = \begin{Bmatrix} q_R \\ q_O \end{Bmatrix} \tag{A3}$$

$$\Phi = \begin{bmatrix} \Phi_R \\ \Phi_O \end{bmatrix} \tag{A4}$$

where the R and O subscripts denote the reduced and omitted DOF, respectively. The reduced displacement vector q_R in Eq. (A3), therefore, can be expressed in Eq. (A5):

$$q_R = \Phi_R\eta \tag{A5}$$

Multiplying Φ_R^T to Eq. (A5) gives Eq. (A6):

$$\Phi_R^T q_R = \Phi_R^T\Phi_R\eta \tag{A6}$$

The generalized coordinate η, therefore, becomes Eq. (A7):

$$\eta = (\Phi_R^T\Phi_R)^{-1}\Phi_R^T q_R = \Psi q_R \tag{A7}$$

where Ψ is obtained using a least-squares fitting in Eq. (A8):

$$\Psi = (\Phi_R^T\Phi_R)^{-1}\Phi_R^T \tag{A8}$$

Substituting Eq. (A7) into Eq. (A2) gives Eq. (A9); an order reduction based on a transformation matrix T is the SEREP.

$$q = \Phi\Psi q_R = Tq_R \tag{A9}$$

Substituting Eq. (A9) into the governing equations of motion in Eq. (A1) gives Eq. (A10):

$$MT\ddot{q}_R + KTq_R = M\Phi\Psi\ddot{q}_R + K\Phi\Psi q_R = 0 \tag{A10}$$

Multiplying $\Psi^T\Phi^T$ to Eq. (A10) gives Eq. (A11):

$$\Psi^T\Phi^T M\Phi\Psi\ddot{q}_R + \Psi^T\Phi^T K\Phi\Psi q_R = M_R\ddot{q}_R + K_R q_R = 0 \tag{A11}$$

The reduced-order mass, M_R, and stiffness, K_R, matrices, therefore, become Eqs. (A12) and (A13), respectively:

$$M_R = \Psi^T\Phi^T M\Phi\Psi = \Psi^T\Psi \tag{A12}$$

$$K_R = \Psi^T\Phi^T K\Phi\Psi = \Psi^T[\omega_n^2]\Psi \tag{A13}$$

Pre- and postmultiplying matrices Φ_R^T and Φ_R to the reduced mass matrix M_R then gives Eq. (A14):

$$\Phi_R^T M_R\Phi_R = \Phi_R^T\Psi^T\Psi\Phi_R \tag{A14}$$

Substituting Eq. (A8) into $\Psi\Phi_R$ in Eq. (A14) gives Eq. (A15):

$$\Psi\Phi_R = (\Phi_R^T\Phi_R)^{-1}\Phi_R^T\Phi_R = I \tag{A15}$$

Equation (A14), therefore, becomes Eq. (A16):

$$\Phi_R^T M_R\Phi_R = I \tag{A16}$$

Similarly, Eq. (A17) is derived from Eqs. (A13 and A15):

$$\Phi_R^T K_R\Phi_R = [\omega_n^2] \tag{A17}$$

The frequencies, therefore, from the ROM, M_R and K_R, are identical with those from the full-order model. When the number of rows, n_{RDOF} of the eigenmatrix Φ_R, is greater than the number of columns (= number of modes m), then there will be zero frequency modes. The number of zero frequency modes will be $n_{RDOF} - m$.

Appendix B: Sensitivity of the Matrix $\Psi = (\Phi_R^T\Phi_R)^{-1}\Phi_R^T$ with Respect to Design Variable x_k

The sensitivity of the matrix Ψ in Eq. (B1) with respect to design variable x_k will be derived in this Appendix:

$$\Psi = (\Phi_R^T\Phi_R)^{-1}\Phi_R^T \tag{B1}$$

Multiplying the matrix $(\Phi_R^T\Phi_R)$ to both sides of Eq. (B1) gives Eq. (B2):

$$(\Phi_R^T\Phi_R)\Psi = \Phi_R^T \tag{B2}$$

Taking the derivative of both sides of Eq. (B2) with respect to the kth design variable, x_k, gives Eq. (B3); therefore, $\partial\Psi/\partial x_k$ becomes Eq. (B4):

$$\frac{\partial(\Phi_R^T\Phi_R)\Psi}{\partial x_k} = \frac{\partial\Phi_R^T}{\partial x_k} = \frac{\partial(\Phi_R^T\Phi_R)}{\partial x_k}\Psi + (\Phi_R^T\Phi_R)\frac{\partial\Psi}{\partial x_k} \tag{B3}$$

$$\begin{aligned}(\Phi_R^T\Phi_R)\frac{\partial\Psi}{\partial x_k} &= \frac{\partial\Phi_R^T}{\partial x_k} - \frac{\partial(\Phi_R^T\Phi_R)}{\partial x_k}\Psi \\ &= \frac{\partial\Phi_R^T}{\partial x_k} - \left(\frac{\partial\Phi_R^T}{\partial x_k}\Phi_R + \Phi_R^T\frac{\partial\Phi_R}{\partial x_k}\right)\Psi\end{aligned} \tag{B4}$$

Multiplying the matrix $(\Phi_R^T\Phi_R)^{-1}$ to both sides of Eq. (B4) gives Eq. (B5):

$$\begin{aligned}\frac{\partial\Psi}{\partial x_k} = {} & (\Phi_R^T\Phi_R)^{-1}\frac{\partial\Phi_R^T}{\partial x_k} - (\Phi_R^T\Phi_R)^{-1}\left(\frac{\partial\Phi_R^T}{\partial x_k}\Phi_R\right. \\ & \left. + \Phi_R^T\frac{\partial\Phi_R}{\partial x_k}\right)(\Phi_R^T\Phi_R)^{-1}\Phi_R^T\end{aligned} \tag{B5}$$

Acknowledgments

The work presented in this paper was funded by the Low-Boom Flight Demonstration Project under the NASA Aeronautics Research Mission Directorate. The author thanks peer review committee members Samson Truong, Benjamin Park, and Scott L. Stebbins of the NASA Armstrong Flight Research Center.

References

[1] Baruch, M., and Bar-Itzhack, I. Y., "Optimal Weighted Orthogonalization of Measured Modes," *AIAA Journal*, Vol. 16, No. 4, 1978, pp. 346–351.
https://doi.org/10.2514/3.60896

[2] Minas, C., and Inman, D. J., "Matching Finite Element Models to Modal Data," *ASME Journal of Vibration and Acoustics*, Vol. 112, No. 1, 1990, pp. 84–92.
https://doi.org/10.1115/1.2930103

[3] Berman, A., and Nagy, E. J., "Improvement of a Large Analytical Model Using Test Data," *AIAA Journal*, Vol. 21, No. 8, 1983, pp. 1168–1173.
https://doi.org/10.2514/3.60140

[4] Schwarz, B., Richardson, M., and Formenti, D. L., "FEA Model Updating Using SDM," *Journal of Sound and Vibration*, Vol. 41, No. 10, 2007, pp. 18–23.

[5] Heylen, W., and Vanhonacker, P., "An Automated Technique for Improving Model Matrices by Means of Experimentally Obtained Dynamic Data," AIAA Paper 1983-0881, 1983.
https://doi.org/10.2514/6.1983-881

[6] Pak, C.-G., "Finite Element Model Tuning Using Measured Mass Properties and Ground Vibration Test Data," *ASME Journal of Vibration and Acoustics*, Vol. 131, No. 1, Feb. 2009, Paper 011009. https://doi.org/10.1115/1.2981092

[7] Pak, C.-G., and Lung, S.-F., "Flutter Analysis of Aerostructures Test Wing with Test Validated Structural Dynamic Model," *Journal of Aircraft*, Vol. 48, No. 4, 2011, pp. 1263–1272. https://doi.org/10.2514/1.C031257

[8] Pak, C.-G., and Truong, S., "Creating a Test-Validated Finite-Element Model of the X-56A Aircraft Structure," *Journal of Aircraft*, Vol. 52, No. 5, 2015, pp. 1644–1667. https://doi.org/10.2514/1.C033043

[9] Juneja, V., Haftka, R. T, and Cudney, H. C., "Location of Damage in a Space Structure by Contrast Maximization," AIAA Paper 1994-1711-CP, 1994. https://doi.org/10.2514/6.1994-1711

[10] Kim, H. M., and Bartkowicz, T. J., "Damage Detection and Health Monitoring of Large Space Structures," AIAA Paper 1993-1705-CP, 1993. https://doi.org/10.2514/6.1993-1705

[11] Zimmerman, D. C., and Simmermacher, T., "Model Refinement and System Health Monitoring Using Data from Multiple Static Loads and Vibration Tests," AIAA Paper 1994-1714-CP, 1994. https://doi.org/10.2514/6.1994-1714

[12] Jaishi, B., and Ren, W. X., "Damage Detection by Finite Element Model Updating Using Modal Flexibility Residual," *Journal of Sound and Vibration*, Vol. 290, Nos. 1–2, 2006, pp. 369–387. https://doi.org/10.1016/j.jsv.2005.04.006

[13] Avitabile, P., "Twenty Years of Structural Dynamic Modification–A Review," *Journal of Sound and Vibration*, Vol. 37, No. 1, 2003, pp. 14–27.

[14] Chen, G., "FE Model Validation for Structural Dynamics," Ph.D. Thesis, Mechanical Engineering Dept., Imperial College London, Univ. of London, London, 2001.

[15] Friswell, M. L., and Mottershead, J. E., *Finite Element Model Updating in Structural Dynamics*, Kluwer, Dordrecht, The Netherlands, 1996, p. 1, Chaps. 7, 8, 9.

[16] *MSC NASTRAN: 2018 Quick Reference Guide*, MSC Software Corp., Newport Beach, CA, 2017.

[17] Pak, C.-G., "Preliminary Development of an Object-Oriented Optimization Tool," NASA TM-2011-216419, 2011.

[18] O'Callahan, J., Avitabile, P., and Riemer, R., "System Equivalent Reduction Expansion Process (SEREP)," *Proceedings of the 7th International Modal Analysis Conference*, Union College, Schenectady, NY, June 1989, pp. 29–37.

[19] Pak, C.-G., "Multiple Shaker Placement for Ground Vibration Test of X-59 Aircraft Using Topology Optimization," *2020 AIAA SciTech Forum*, AIAA Paper 2020-1901, 2020.

[20] Doyle, S., Robinson, J., Ho, V., Ogawa, G., and Baker, M., "Aeroelastic Optimization of Wing Structure Using Curvilinear Spars and Ribs (SpaRibs) and SpaRibMorph," *58th AIAA/ASCE/AHS/ASC Structures, Structural Dynamics, and Materials Conference*, AIAA Paper 2017-1303, Jan. 2017. https://doi.org/10.2514/6.2017-1303

[21] *ZAERO User's Manual: Version 9.2*, ZONA Technology, Inc., Scottsdale, AZ, 2017.

[22] Haug, E. J., and Arora, J. S., *Applied Optimal Design*, John Wiley & Sons, Inc., New York, 1979, pp. 55, 112.

[23] Pak, C.-G., "Unsteady Aerodynamic Model Tuning for Precise Flutter Prediction," *Journal of Aircraft*, Vol. 48, No. 6, 2011, pp. 2178–2184. https://doi.org/10.2514/1.C031495